Nuclear Instruments and Methods in Physics Research A 1058 (2024) 168796

Contents lists available at ScienceDirect

Nuclear Inst. and Methods in Physics Research, A

journal homepage: www.elsevier.com/locate/nima

Integration and first operation of the Gotthard-II detector at European XFEL

Marco Ramilli [a,*], Karim Ahmed [a], Raphael de Wijn [a], Thomas Dietze [a], Bruno Fernandes [a], David Hammer [a], Yifeng Jiang [a], Dmitry Khakhulin [a], Jayanath C.P. Koliyadu [a], Romain Letrun [a], Jia Liu [a], Carlos Lopez-Cuenca [b], Davide Mezza [b], Christopher Milne [a], Aldo Mozzanica [b], Andrea Parenti [a], Tokushi Sato [a], Philipp Schmidt [a], Bernd Schmitt [b], Marcin Sikorski [a], Monica Turcato [a], Yohei Uemura [a], Hao Wang [a], Hazem Yousef [a], Jiaguo Zhang [b]

[a] European XFEL, Holzkoppel 4, Schenefeld, 22869, Germany
[b] Paul Scherrer Institut, Forschungsstrasse 111, Villigen, 5232, Switzerland

ARTICLE INFO

Keywords:
X-ray detectors
MHz detectors
FEL
Integration
Calibration

ABSTRACT

Gotthard-II (G-II) is a 1-D silicon microstrip hybrid detector developed by the Paul Scherrer Institut within the framework of a collaboration agreement with the European XFEL. The ASIC features a dynamic gain switching architecture, in order to cope with the luminosity of European XFEL, and a 12-bit analog-to-digital converter with a sampling/conversion rate of more than 18 MS/s as well as a Static random-access memory, making it capable of matching the European XFEL pulse train structure, thus acquiring up to 2700 images at 4.5 MHz per burst. The sensor's strip pitch can be either of 50 μm or 25 μm , for a total of 1280 or 2560 output channels per detector, respectively, with a spectral sensitivity that allows either X-ray detection (optimized in the 5–20 keV range) or visible light detection. Its exceptionally good compliance with the European XFEL beam conditions will make G-II the most widely employed detector across the facility, with a total of 29 modules of different flavors that will be installed in scientific instruments and beam diagnostic setups. Although the detector will be predominantly used for spectroscopic measurements it will have a variety of other applications, including X-ray diffraction/emission/absorption experiments, relative pulse arrival time monitoring (of fundamental importance for pump–probe experiments), spectral diagnostics, and beam quality monitoring, with the possibility for the detector itself to generate a veto patterns for the large area MHz framerate pixel detectors employed at the scientific instruments, such as AGIPD, LPD and DSSC. In this paper, an overview of G-II detector technology and its usage at the European XFEL will be presented; the focus will then move on towards the process of detector integration in the European XFEL control system, data acquisition, and data correction infrastructure, highlighting its challenges. Finally, an overview of the first results obtained at scientific instruments will be given.

1. Introduction

The European X-ray Free Electron Laser (European XFEL) is a cutting-edge research facility located in the Hamburg metropolitan region of Germany [1]. Its superconducting linear accelerator produces electron bunches with an energy of up to 17.5 GeV, arranged in 10 Hz trains with up to 2700 bunches per train with a maximum intra-bunch repetition rate of 4.5 MHz. Each train lasts for 0.6 ms and is followed by a gap of 99.4 ms. Spatially coherent X-rays are generated from the electron bunches using the Self-Amplified Spontaneous Emission (SASE) process in a series of undulators. The X-rays are produced in three photon beamlines, which extend over a length of up to 200 m, providing X-rays in the energy range from 300 eV to over 25 keV. The SASE1 and SASE2 beamlines serve two instruments, while the SASE3 beamline serves three instruments, each with different scientific goals.

The X-ray pulses produced by the European XFEL have the same structure in time as that of the electron bunches and are extremely intense and ultra-short, with pulse lengths of less than 100 fs and a peak brilliance that is a billion times higher than conventional synchrotron radiation sources. These features pose unique challenges for the detector systems used at the European XFEL. The scientific instruments require detectors that are specifically optimized for their individual requirements, such as photon energy range, noise, dynamic range, spatial resolution, and operation in vacuum or ambient environments. The AGIPD [2], DSSC [3] and LPD [4] detectors have

* Corresponding author.
E-mail address: marco.ramilli@xfel.eu (M. Ramilli).

https://doi.org/10.1016/j.nima.2023.168796
Received 15 May 2023; Received in revised form 12 October 2023; Accepted 14 October 2023
Available online 17 October 2023

been developed specifically for the European XFEL and are now in use at the SPB/SFX [5], MID [6] and HED [7] (AGIPD), SCS [8] and SQS [9] (DSSC), and FXE [10] (LPD) instruments, respectively. Similarly, different user cases highlighted the necessity of a detector for energy dispersive measurements compatible with the European XFEL pulse train structure; examples may be HIgh REsolution hard X-ray single-shot spectrometer (HIREX) for photon diagnostic [11], the Photon Arrival time Monitor (PAM) [12], or the spectroscopic camera for the novel MHz-Tomoscopy Project [13]. This led to the development of the Gotthard-II (G-II) detector, whose main characteristics will be outlined in the following Section 2.

2. The Gotthard-II detector

The G-II detector has been developed at the Paul Scherrer Institut (PSI)[1] in the framework of a collaboration agreement with the European XFEL. The aim of the collaboration was to develop a detector aimed mainly at energy dispersive measurements, compatible with the pulse train structure of the European XFEL, i.e. capable of acquiring up to 2700 images per train at a frame rate of 4.5 MHz. Additionally, each channel should feature a dynamic range of about 10^4 12 keV photons, while still maintaining single photon resolution capabilities.

2.1. ASIC operation and calibration

The working principles of the G-II readout ASIC and its calibration are extensively described in [14]: its fundamental aspects, most directly impacting the detector integration and operation will be here recalled and summarized.

The output of the sensor strip is read out by a charge sensitive pre-amplifier (PRE) featuring a dynamic gain switching (DGS) architecture. Three feedback capacitors with different capacitance are implemented, and are in turn inserted in the feedback loop when the PRE output exceeds a threshold value set in a comparator connected to the PRE output; the status of the gain switching mechanism is encoded in two bits. With the addition of further feedback capacitance the amplification of the PRE is therefore reduced, consequently diminishing its signal resolution capabilities, but allowing it to integrate more charge. The amplification of the highest gain setting G0 is such that single photon resolution is possible at photon energies above 5 keV with a signal-to-noise ratio better than 5, according to the noise estimate provided by the detector calibration; subsequent gain stages G1 and G2 allow to extend the dynamic range enough to satisfy the original requirements stated above.

The output of the PRE is stored in two sets of analog storage cells, in turn sampling the output of even or odd images, and therefore identified with the EVEN or ODD label.

Four channels are multiplexed to one fully differential Correlated Double Sampling (CDS) stage; the CDS block operates at a 18 MHz sampling rate, converting the single-ended output of the previous block into a fully differential signal. The CDS output is then connected to an Analog-to-Digital Converter (ADC) for on chip digitization; the ADC employed on the G-II ASIC is a fully differential asynchronous Successive Approximation Register (SAR) ADC, providing a 12-bit raw output.

Finally, the ADC output together with the bit encoding of the gain switching mechanism is stored in a Static Random-Access Memory (SRAM) with a memory depth of 2720 images, therefore fully capable of acquiring an image for every pulse of a European XFEL pulse train.

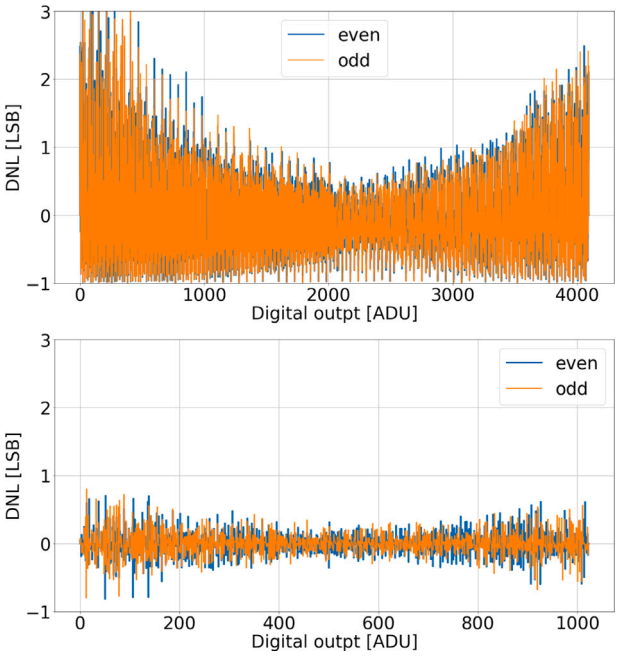

Fig. 1. Top: an example of the DNL calculated for a particular strip of a G-II module, for both the even and odd storage cell blocks. Bottom: the DNL for the same strip, after linearization and compression to 10 bit; the range of the y-axis is kept the same to highlight the improvement in the DNL.

2.1.1. ASIC calibration

In order to convert the raw output of the detector into physical units, three basic sets of calibration constants need to be determined; the procedure to obtain each one of these is described in detail in [14], and a summary is presented here.

1. **ADC linearization**. The raw 12-bit output of the ADC is non-linear due to the mismatch of capacitance in the DAC array of the ADC as well as the parasitic one: Fig. 1 shows an example of the differential non-linearity (DNL) for one G-II channel. In addition, it shows an elevate number of missing ($DNL[i] = -1$) or stuck ($DNL[i] > 1$) codes (where i indicates the ith code of the 12-bit ADC output). The linearization is performed via:

$$Dout_{10\ \mathrm{bit}}[i] = (Dout_{12\ \mathrm{bit}} + INL[i])/4 \tag{1}$$

which also operates a compression from 12 to 10 bit. In Eq. (1), $Dout$ are the digital output at 12 and 10 bit, respectively, and $INL[i]$ indicates the ith code of the integral non-linearity calculated as:

$$INL[i] = \sum_{j=1}^{i} DNL[j]. \tag{2}$$

Eq. (1) provides a look-up table (LUT) that maps each of the 4096 codes of the 12-bit ADC output into its 1024 linearized 10-bit correspondent.

2. **Gain conversion map**. Gain conversion factor from ADC units to keV must be obtained on a channel-by-channel basis, for each set of storage cells and for each one of the three gain stages. For G0 the constants are directly measured using flat field illumination with photons of known energy (e.g. Cu K_α fluorescence), in single-photon regime. Gain conversion factors for lower gains G1 and G2 are calculated by measuring the gain ratios $G0/G1$ and $G1/G2$ from the ratio of the slopes in the G-II

[1] https://www.psi.ch.

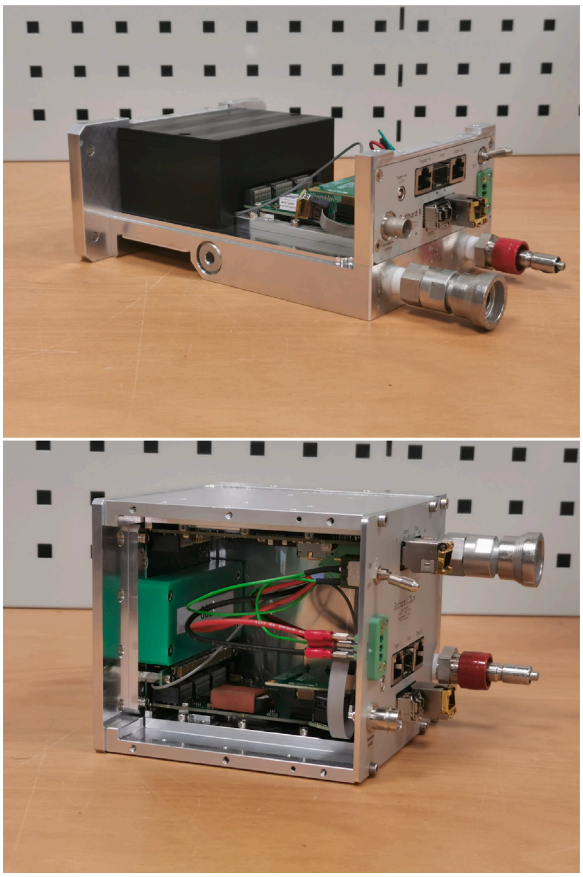

Fig. 2. Top: a G-II with 50 μm pitch; the cover is removed and the Main Board can be seen. Bottom: a G-II with 25 μm pitch sensor: the two Main Boards can be seen connected from opposite sides of the FEM.

response curve to a dynamic range scan performed with external charge injection into the sensor.

3. **Offset map**. Offsets are the estimate of the pedestal output of the detector, to be subtracted from raw data before gain conversion; these constants need also to be evaluated for each channel, storage cell set and gain stage. Offsets for G0 are calculated from the average of images taken without illumination (so called *dark runs*), while for G1 and G2 are obtained from the offset of the linear fit of the dynamic range scan used for gain calibration.

Both offsets and gain conversion factors are calculated after ADC linearization, for a total of twelve calibration constants per channel.

2.2. Detector modules

The G-II modules in their 50 μm and 25 μm strip-pitch variants are shown in Fig. 2. One G-II ASIC hosts 128 individual channels and ten ASICs are used together to form a front-end module (FEM) with a total of 1280 channels; in case of the 25 μm version, the FEM is equipped with double the ASICs. FEMs are controlled and read out by a Main Board (MB), equipped with an Intel Cyclone 10 GX(CX) FPGA. The MB is powered by a +12 V supply, while the sensor is biased by a DC-DC converter mounted on the MB, capable of generating up to 560 V. The MB is equipped with two 10 Gb/s interfaces, of which one is used for slow control (with a 1 Gb/s transceiver) and the other for sending the data out of the module, with a 10 Gb/s SFP+ transceiver.

A single MB is used to read out the output of ten ASICs: in case of a sensor segmented into strips with 50 μm pitch only one MB is used, while in case of the 25 μm strip pitch version, two MBs are needed, each one reading out the output of ten of the twenty ASICs composing the FEM. The sensor strips are connected to the FEM by wire-bonding them in an interleaved mode (i.e. strip_0 to channel_0 of FEM_0, strip_1 to channel_{1279} of FEM_1 and so on). The two MBs are operating in a master and slave configuration, with two interfaces for slow control and two for data out.

To synchronize the detector operation to the European XFEL time structure, each module is equipped with a timing board, which receives the European XFEL clock, the train trigger and the train metadata; more information is provided in Section 2.3.

More details on the readout electronics and the mechanics of the detector modules will be described in a dedicated scientific communication currently in preparation.

2.3. European XFEL timing system integration

The European XFEL timing system is implemented using a MicroTCA NAMC-psTimer AMC board [15], initially developed at DESY [16], and follows the concept of event and reference clock distribution. A master board receives an external clock reference and distributes encoded train metadata information via fiber-optic links to other timing systems present in the facility and beamlines. The bit rate matches the clock reference and the board includes dedicated hardware to measure the phase delay between the locally regenerated clock and the original source.

The information distributed includes the Train ID, a unique 64-bit number to identify the current train, a table of triggers to generate with respect to the beginning of a 10 Hz cycle and locally compensated to include the delay of the fiber communication, as well as the bunch table, which describes the charge, destination, and other characteristics of a bunch present in a train. Decoding takes place in a Xilinx FPGA, with the information being used to generate triggers and clocks in the board interface according to the requirements of the user.

3. The Karabo control system

The Karabo distributed control system [17] has been developed in-house at the European XFEL in order to address its challenging requirements in terms of controlling complex and custom-made hardware, transferring large amounts of data, and integrating data analysis workflows. Karabo interfaces to hardware device through software counterparts called ‘Karabo Devices’; three different APIs are available, the ‘C++’ one, a ‘Python’ one based on ‘C++’ bindings, and a purely “pythonic” one.

The internal communication in the Karabo control system is done via a message broker. An important difference with respect to many other control systems is that in Karabo the updates are event-driven: only if a change in a device property or state occurred, will the update be distributed via the message broker. The interested devices do not need to poll to receive updates; they only subscribe to the broker’s updates.

In addition to the broker-based communication, the control system also provides peer-to-peer messaging between devices. This is used to transfer larger amounts of data, e.g. from detectors to calibration pipelines and data storage.

The Karabo control system provides data logging capabilities too. The device properties are logged in a time series database and can be retrieved via a web interface.

The main interaction point for the operator is the Karabo GUI (Fig. 3). The operator can save a list of Karabo devices to be started and their settings in so-called “projects”. The right-hand tab in the GUI displays all the device properties and allow to set the reconfigurable ones. It also allows to execute commands on the device. Custom user interfaces, termed scenes, can be created by dragging and dropping device properties or commands in the middle tab; scenes can be saved to the project too.

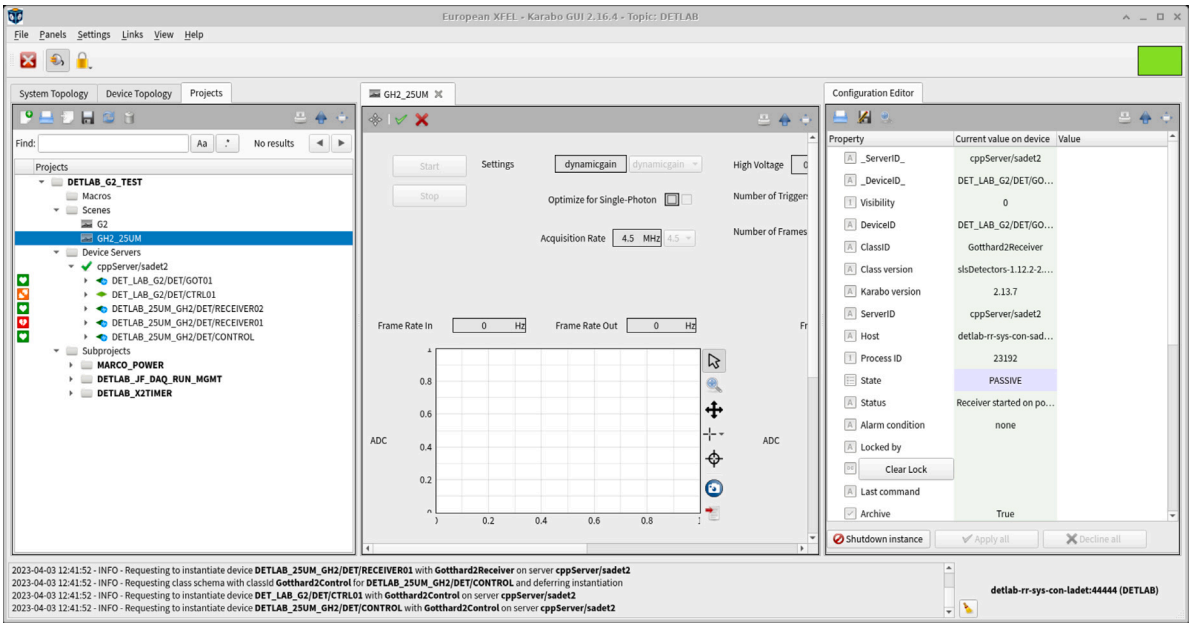

Fig. 3. The Karabo GUI. In the left-hand tab the project view is visible, in the middle one the custom scene for a G-II, on the right-hand side the detailed view of a Karabo device.

3.1. Karabo integration

Karabo software devices have been developed to support the Gotthard, Jungfrau and G-II detectors, based on the C++ API provided by the slsDetectorPackage.[2] Two C++ base classes have been written, one for the detector control and one for receiving the data. From them a specific class for each supported detector type is derived.

At the European XFEL multiple detector modules can be controlled by a single Karabo control device, but there will be a receiver per module. Each Karabo receiver device will unpack the raw data on-the-fly in ADC and gain values, and then it will stream them to the Karabo GUI and the European XFEL data acquisition (DAQ) system using peer-to-peer connections. The DAQ system has the task of matching data from different sources having the same timestamp, and storing them in HDF5 files [18]. The calibration of the data and merging of different modules in a single image are done after the DAQ.

4. Calibration effort at european XFEL

European XFEL aims to provide facility users with a scientifically utilizable dataset as the primary data product. To this end, online and offline calibration infrastructure is developed by, deployed at, and supported by the facility.

The online correction pipelines provide a real-time preview of corrected detector output with the option to stream this data to other facilities- or user-provided online analysis tools. The latter offline infrastructure enables flexible and reproducible high-quality corrections of stored data for later scientific analysis up to publication. Additionally, this system facilitates the generation of calibration constants used for the corrections in both the online and offline settings. In the case of G-II , these comprise the 10-bit compression LUT described in Section 2.1.1, offset (pedestal) values, and gain correction values. It also includes a bad pixel mask signifying any extraordinary conditions present in a given pixel and frame, e.g. excessive noise detected the characterization process or an invalid value encountered in the data stream.

4.1. Online correction

For online correction, a detector-specific Karabo software device was developed for G-II correction. It processes the raw ADC data received either directly from the receiver device or via a DAQ device to produce a number of preview outputs in addition to full-speed corrected data. The previews provide raw and corrected data for both single frames as well as optional reductions across frames, which in the case of G-II are vectors, along with a streak preview concatenating multiple vector frames of a given train into an image. Fig. 4 illustrates how multiple of these previews can be displayed in a custom scene within the Karabo GUI. In order to correct data at full speed, the device uses a single custom *Cython*-based correction function which applies the LUT, offset correction, gain correction, and bad pixel masking in a single pass. Since the calibration constants are produced on a FEM basis, for a single 50 μm detector installation, a single correction device suffices to provide a correction pipeline capable of providing preview outputs and full-speed corrected data for downstream use. For the 25 μm installations, two correction devices are deployed, each independently correcting the data it receives from each FEM as if it were from a standalone 50 μm detector. The fast outputs from the two correction devices are passed through an additional Karabo software device which interleaves them along the pixel axis to create the full data stream. Similarly, for each of the preview outputs, an additional purpose-built device is deployed to interleave the respective 1D or 2D previews, enabling complete previewing in the Karabo GUI. This topology mirrors the multi-device data flows used for modular 2D detectors already installed at European XFEL like AGIPD, LPD, and DSSC and so allows for the reuse of existing high-level pipeline management devices in the online correction software to automate the instantiation and configuration of multi-device pipelines.

4.2. Offline calibration

The offline calibration process is a Python-based pipeline leveraging the Maxwell HPC[3] cluster to apply corrections on large file-based data volumes as well as generate the necessary calibration data used both here and for the aforementioned online corrections. Rather than

[2] https://slsdetectorgroup.github.io/devdoc/index.html.

[3] https://confluence.desy.de/display/MXW/.

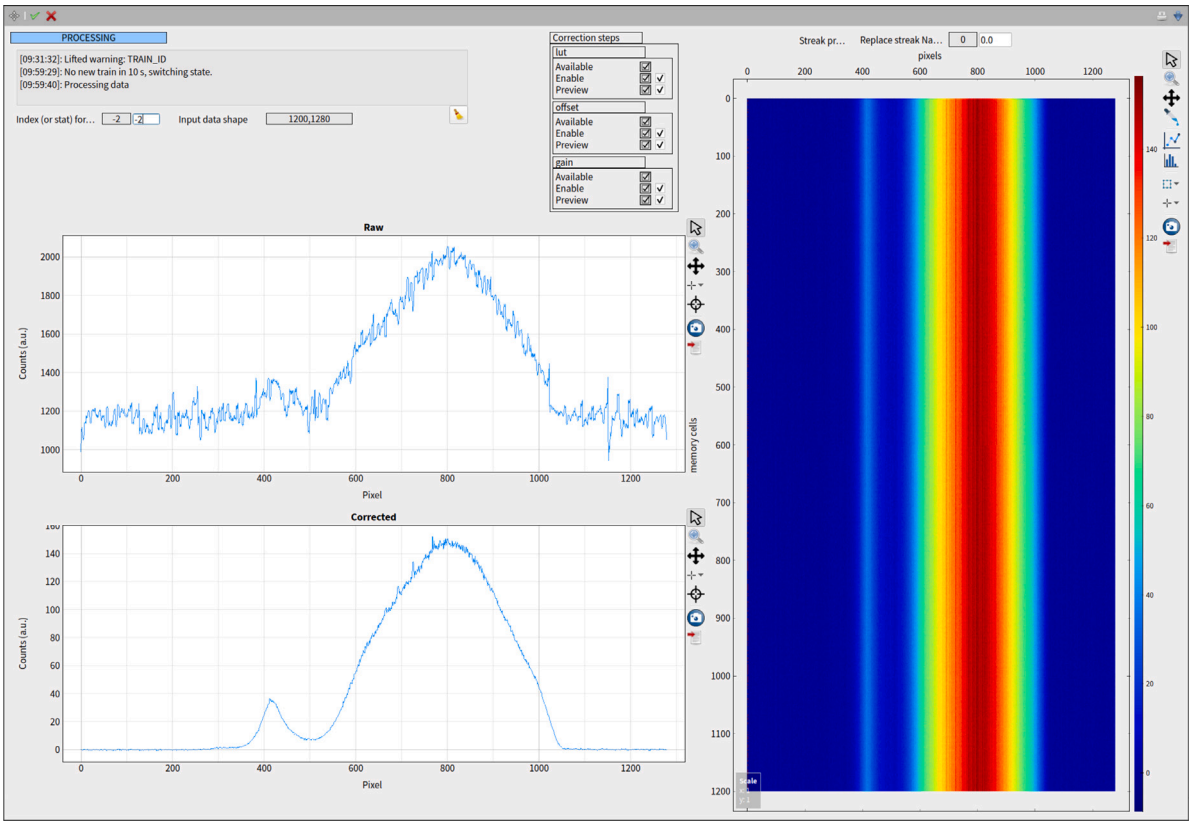

Fig. 4. Screenshot from a custom scene within the Karabo GUI displaying the raw, corrected, and stream outputs provided by a G-II correction device. Included in the scene are controls to choose which frame (or which statistic computed across frames) to display on the 1D previews along with toggles for individual correction steps. Note that each correction step can be enabled or disabled independently for preview and full data outputs, allowing operators and users of online analysis to omit certain corrections if needed.

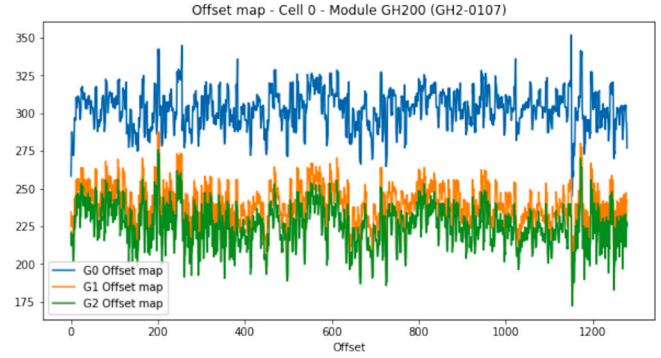

Fig. 5. Shown here is a 1D plot from an offline calibration PDF report, automatically generated as a part of the dark processing for generating offset and dark bad pixels for a 50 μm G-II detector at the SPB/SFX instrument. The offset map is computed across both storage cells and for the 3 gains, but the plot displays the offset map for the odd cells only.

aiming for low latency, it is designed to produce high-quality data in a flexible and reproducible manner across all its processing steps. It is available through the web interface used to manage all user data taken at European XFEL (Metadata Catalogue), where a user may select data for corrections as well as detector characterization to produce calibration data. This calibration data is then stored in a database (Calibration Catalogue) indexed by a unique FEM identifier and its operation condition and can be retrieved at any time for corrections. After a processing job is finished, a PDF report is generated to document each step and its results (see Fig. 5). The offline pipeline for G-II detector data correction is similar to the online correction process. It involves converting 12-bit raw data to 10-bit data using LUT parameters and then performing offset and gain correction. Additionally, bad pixel parameters are masked during the correction process. In terms of data storage, the offline correction for G-II stores the result in the same HDF5 data structures as all raw data at European XFEL. However, unlike the 50 μm detector, which appears as a single data source for both raw and corrected data, the 25 μm detector is interleaved into a single data source after corrections to appear as a singular detector for data analysis.

5. First experimental tests

5.1. X-ray emission spectroscopy

The first end-to-end test of a fully integrated detector was performed at the FXE instrument of the European XFEL. The test had several goals:

1. test the whole integration in a realistic experimental situation;
2. test non-standard operation modes, i.e. reduced clock frequency to acquire at 1.1 MHz burst frame rate and increased CDS amplification to improve the signal-to-noise ratio;
3. perform pump–probe X-ray emission spectroscopy (XES) measurements to evaluate the detector performances.

For this purpose, the detector was mounted on a robotic arm as part of the Von Hamos spectrometer installed at the FXE instrument [19]. In order to perform G0 gain stage calibration with high CDS amplification (CDS1), the detector was exposed to a weak flat field illumination of Cu K_α fluorescence to ensure the single photon detection regime in each frame. The results have been compared with the standard setting of low CDS amplification (CDS0) using the calibration procedure described in Section 2.1.1, and exemplified in Fig. 6. From Fig. 7 (top) it can be observed that in average the CDS1 setting provides a 30% higher gain

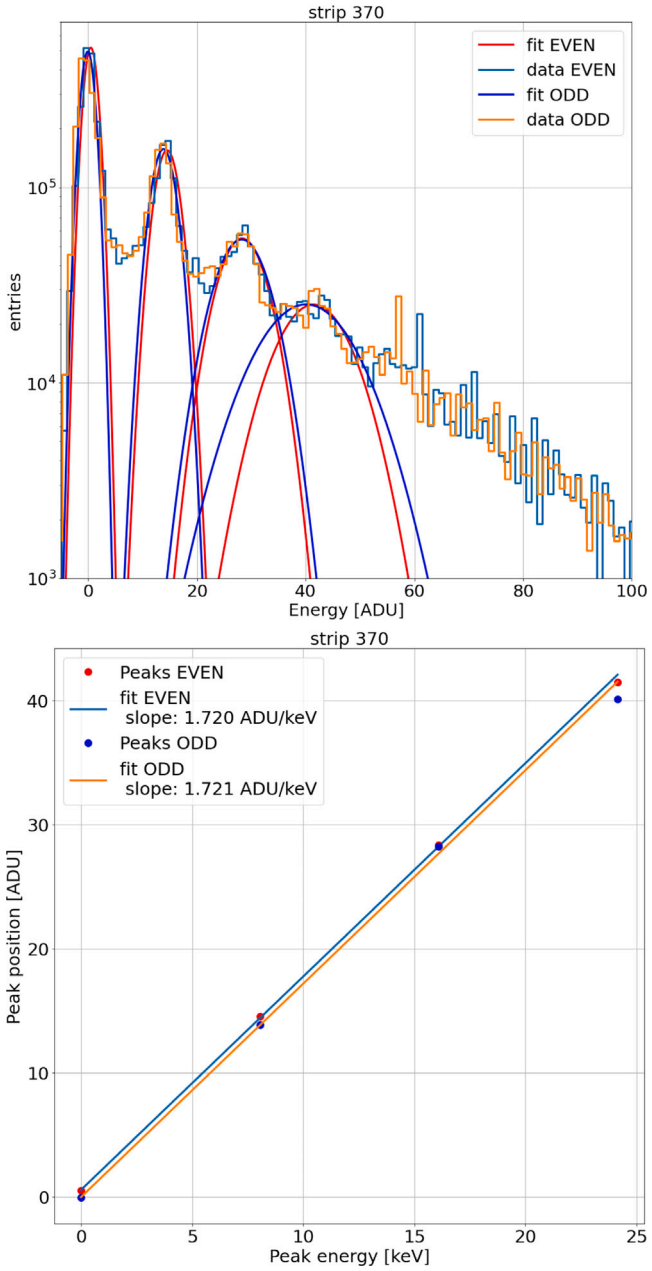

Fig. 6. Top: Cu K_α spectrum for even and odd storage cell blocks for a single strip; in red and blue are depicted the Gaussian fit used to estimate the peak positions. Bottom: the linear fit of the peak position against the peak energy used to calculate the gain conversion factor.

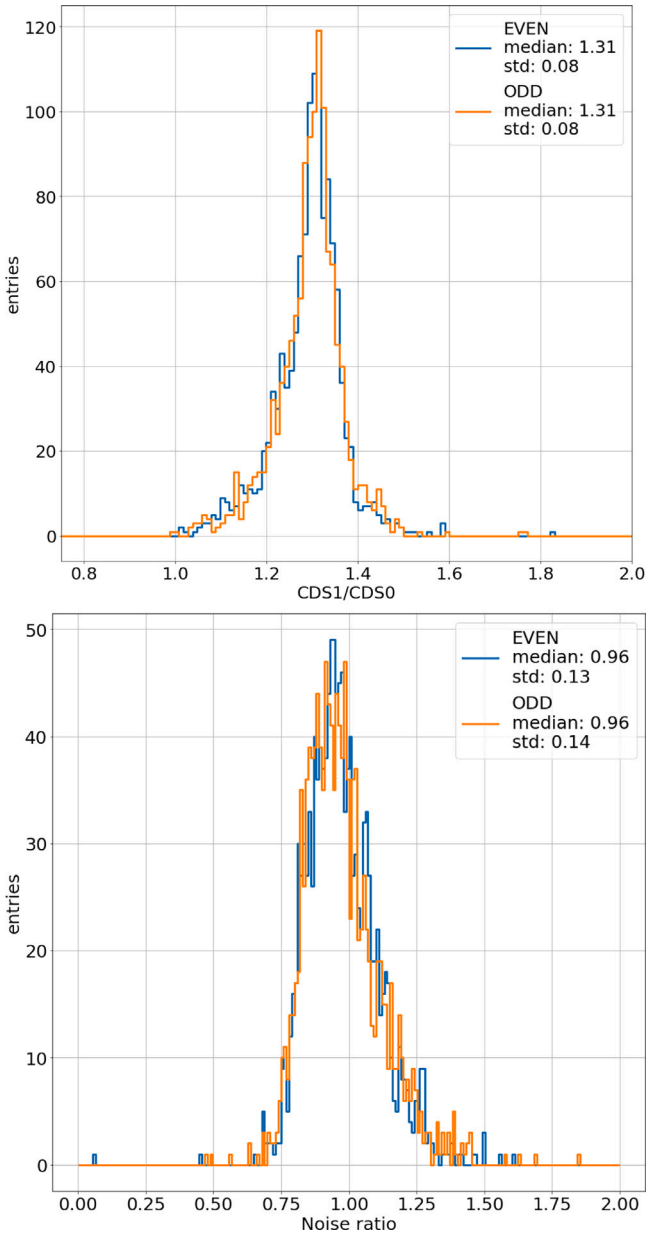

Fig. 7. Top: the ratio between the G = gain conversion factors with the CDS1 setting with respect to the CDS0 setting(default). Bottom: ratio between the noise figures calculated with CDS1 and 1.1 MHz frame rate, and the standard settings.

conversion factor. Using the variance of the pedestal peak as an estimate of the noise, it can also be concluded that the noise performances of the detector at 1.1 MHz with CDS1 setting are similar to the default settings (i.e. CDS0 and 4.5 MHz frame rate), as demonstrated by the ratio of the noise values obtained in these two configurations shown in Fig. 7 (bottom). Therefore, a 30% improvement in the signal-to-noise ratio can be obtained the CDS1 operation mode.

For the test experiment, a 30 mM solution of tris(acetylacetonato) cobalt(III) ($Co(acac)_3$) in acetonitrile was delivered to the interaction region via a fast cylindrical jet (100 μm jet diameter), and Co $K_{\alpha_{1,2}}$ X-ray emission spectra were detected with G-II for every pulse at 564 kHz intra-train repetition rate, which was limited by the sample refresh rate in the interaction region. In this pump-probe experiment the solution jet was excited by 400 nm femtosecond pulses at repetition rate of 282 kHz, i.e. for every other X-ray pulse within each pulse train with a total number of 140 and 70 pulses per train for X-rays and optical laser respectively. Thus the Laser On and Laser Off conditions were alternated on a per-pulse basis. The results have been compared with the ones obtained in the same experiment using the Jungfrau 1 Megapixel (JF1M) camera [20], which is the default detector for this installation at FXE [19]. The JF1M does not possess the frame rate capabilities of the G-II detector, so the Laser On and Laser Off conditions were alternated per-train for JF1M, i.e. all pulses in every other X-ray train were with the Laser On and otherwise with Laser Off setting. Spectra recorded by the G-II and averaged over the Laser On and Off subsets of frames for a 250 fs pump-probe delay are shown in Fig. 8 together with their normalized difference. A comparison with the same experiment conducted with the JF1M shows only minor differences, whose origin might be related to the different acquisition schemes and will be systematically investigated in follow-up measurements.

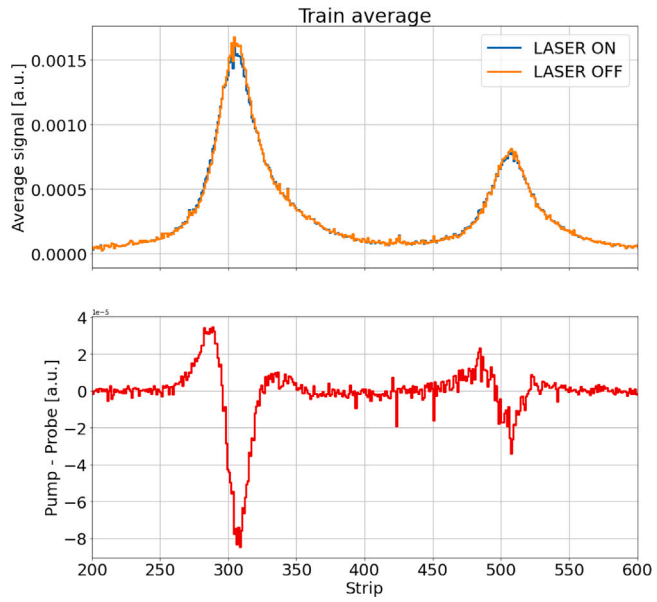

Fig. 8. Top: The average of Co $K_{\alpha_{1,2}}$ lines with pump laser on and off at 250 fs pump-probe delay. To take the pulse-by-pulse intensity fluctuations into account, the G-II output has been weighted with the output of an X-ray Gas Monitor (XGM) [21], which measures pulse intensity. Bottom: the difference between average G-II signal with Laser On and with laser Off produced after additional normalization to the total intensity of respective average spectra.

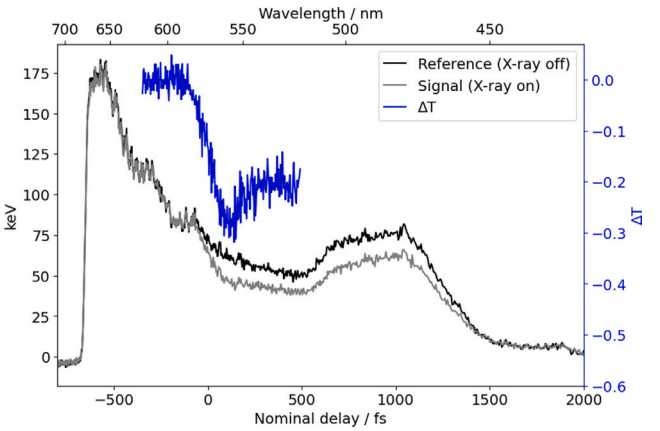

Fig. 9. Examples of Signal and Reference spectra as measured with the PAM equipped with a G-II detector. In blue the ΔT is also plotted.

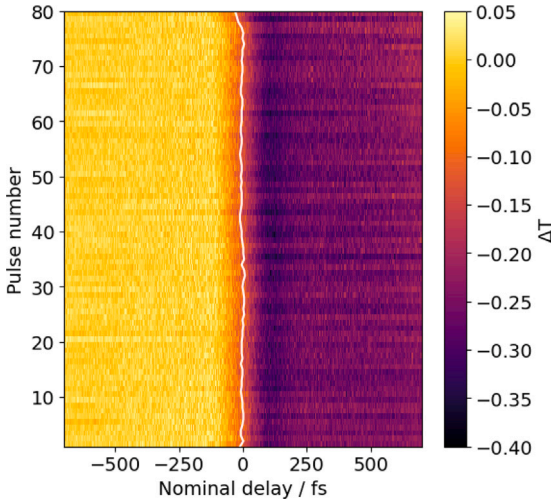

Fig. 10. Example of a single-shot measurement of the X-ray pulse delay with respect to the PP laser within a pulse train.

5.2. Photon arrival time monitor

A G-II module with visible light sensitive sensor was installed in the Photon Arrival time Monitor (PAM) installed at the SPB/SFX scientific instrument of the European XFEL; the setup was developed by the X-ray Photon Diagnostic (XPD) group. The details of the PAM setup are addressed in [12], here the basic principles of operations will be recalled.

The PAM employs the spectral encoding method [22] to measure the relative delay between the pump–probe (PP) laser and the X-ray pulses of European XFEL. The PP laser is used to generate a supercontinuum for a broader bandwidth, which then passes through a dielectric target material and the transmitted beam is coupled into a spectrometer and then detected by 1-D detector: previous version of the PAM employed two Gotthard-I detectors [23]. The interaction of X-ray pulses with the dielectric target changes its refractive index, which in turn results in a change of transmission of the PP laser. This change, encoded in the PP laser spectrum, provides a measurement of the relative time difference between the PP laser and X-ray pulses. Fig. 9 shows an example of Signal (i.e. with X-ray interaction) and Reference (i.e. without X-ray interaction) spectra, along with the modulated spectrum defined as $\Delta T = \text{Signal/Reference} - 1$. With the upgrade to a G-II the SPB/SFX PAM setup has become capable of measuring single-shot arrival time jitter at a X-ray repetition rate of 2.25 MHz, a strong improvement over the previous version of the setup [12,24,25]. As an example, Fig. 10 shows a measurement of arrival times of 80 intra-pulses within a pulse train at 1.13 MHz. Concerning the time resolution and measurement uncertainty of the setup, a precise evaluation is still ongoing and will be addressed in subsequent communications.

6. Conclusions

The Gotthard-II detector is a hybrid strip detector developed by the PSI with the aim of providing a detector capable of fully exploiting the unique time structure of X-ray pulses delivered by the European XFEL machine, which means that it should be able to acquire up to 2700 images per bunch train, at a intra-burst repetition rate of 4.5 MHz. The first G-II modules endowed with 50 μm pitch silicon sensor have been delivered and fully integrated in the Karabo control system and in the signal correction pipeline (both online and offline). The first tests performed at the scientific instruments FXE and SPB/SFX in realistic experimental conditions demonstrate the successful integration. In particular, the PAM tests conducted at SPB/SFX demonstrate that the detector satisfies its design requirements concerning the compatibility with the European XFEL bunch pattern structure. The measurements conducted at FXE have been used to test non-standard operation modes (high CDS gain, 1.1 MHz frame rate), and to perform pump-probe femtosecond XES with $Co(acac)_3$ complex in solution. Results of the G-II pulse-resolved XES measurements have been compared with static XES measurements performed with the Jungfrau 1 Megapixel detector; some differences have been noted in the results, and their origin will be further investigated in follow up measurements.

The successful integration tests open the way to a more streamlined installation process for the upcoming modules. User operation at the European XFEL will significantly benefit from the improved diagnostics offered by G-II [11], particularly in terms of photon timing and self-seeding capabilities. Additionally, scientific applications which require pulse-by-pulse spectroscopic information like the MHz-Tomoscopy project [13], will experience a substantial enhancement with the deployment of this advanced detector version.

Declaration of competing interest

The authors declare the following financial interests/personal relationships which may be considered as potential competing interests: The authors declare that the research was conducted in the absence of any commercial or financial relationships that could be construed as a potential conflict of interest.

Acknowledgments

The authors would like to acknowledge the contribution of the European XFEL and in particular of the scientific instruments SPB/SFX and FXE for the beam time allocations, preparation and support during operation.

References

[1] W. Decking, S. Abeghyan, P. Abramian, A. Abramsky, A. Aguirre, C. Albrecht, P. Alou, M. Altarelli, P. Altmann, K. Amyan, V. Anashin, E. Apostolov, K. Appel, D. Auguste, V. Ayvazyan, S. Baark, F. Babies, N. Baboi, P. Bak, V. Balandin, R. Baldinger, B. Baranasic, S. Barbanotti, O. Belikov, V. Belokurov, L. Belova, V. Belyakov, S. Berry, M. Bertucci, B. Beutner, A. Block, M. Blöcher, T. Böckmann, C. Bohm, M. Böhnert, V. Bondar, E. Bondarchuk, M. Bonezzi, P. Borowiec, C. Bösch, U. Bösenberg, A. Bosotti, R. Böspflug, M. Bousonville, E. Boyd, Y. Bozhko, A. Brand, J. Branlard, S. Briechle, F. Brinker, S. Brinker, R. Brinkmann, S. Brockhauser, O. Brovko, H. Brück, A. Brüdgam, L. Butkowski, T. Büttner, J. Calero, E. Castro-Carballo, G. Cattalanotto, J. Charrier, J. Chen, A. Cherepenko, V. Cheskidov, M. Chiodini, A. Chong, S. Choroba, M. Chorowski, D. Churanov, W. Cichalewski, M. Clausen, W. Clement, C. Cloué, J.A. Cobos, N. Coppola, S. Cunis, K. Czuba, M. Czwalinna, B. D'Almagne, J. Dammann, H. Danared, A. de Zubiaurre Wagner, A. Delfs, T. Delfs, F. Dietrich, T. Dietrich, M. Dohlus, M. Dommach, A. Donat, X. Dong, N. Doynikov, M. Dressel, M. Duda, P. Duda, H. Eckoldt, W. Ehsan, J. Eidam, F. Eints, C. Engling, U. Englisch, A. Ermakov, K. Escherich, J. Eschke, E. Saldin, M. Faesing, A. Fallou, M. Felber, M. Fenner, B. Fernandes, J.M. Fernández, S. Feuker, K. Filippakopoulos, K. Floettmann, V. Fogel, M. Fontaine, A. Francés, I.F. Martin, W. Freund, T. Freyermuth, M. Friedland, L. Fröhlich, M. Fusetti, J. Fydrych, A. Gallas, O. García, L. Garcia-Tabares, G. Geloni, N. Gerasimova, C. Gerth, P. Geßler, V. Gharibyan, M. Gloor, J. Głowinkowski, A. Goessel, Z. Gołębiewski, N. Golubeva, W. Grabowski, W. Graeff, A. Grebentsov, M. Grecki, T. Grevsmuehl, M. Gross, U. Grosse-Wortmann, J. Grünert, S. Grunewald, P. Grzegory, G. Feng, H. Guler, G. Gusev, J.L. Gutierrez, L. Hagge, M. Hamberg, R. Hanneken, E. Harms, I. Hartl, A. Hauberg, S. Hauf, J. Hauschildt, J. Hauser, J. Havlicek, A. Hedqvist, N. Heidbrook, F. Hellberg, D. Henning, O. Hensler, T. Hermann, A. Hidvégi, M. Hierholzer, H. Hintz, F. Hoffmann, M. Hoffmann, M. Hoffmann, Y. Holler, M. Hüning, A. Ignatenko, M. Ilchen, A. Iluk, J. Iversen, J. Iversen, M. Izquierdo, L. Jachmann, N. Jardon, U. Jastrow, K. Jensch, J. Jensen, M. Ježabek, M. Jidda, H. Jin, N. Johansson, R. Jonas, W. Kaabi, D. Kaefer, R. Kammering, H. Kapitza, S. Karabekyan, S. Karstensen, K. Kasprzak, V. Katalev, D. Keese, B. Keil, M. Kholopov, M. Killenberger, B. Kitaev, Y. Klimchenko, R. Klos, L. Knebel, A. Koch, M. Koepke, S. Köhler, W. Köhler, N. Kohlstrunk, Z. Konopkova, A. Konstantinov, W. Kook, W. Koprek, M. Körfer, O. Korth, A. Kosarev, K. Kosiński, D. Kostin, Y. Kot, A. Kotarba, T. Kozak, V. Kozak, R. Kramert, M. Krasilnikov, A. Krasnov, B. Krause, L. Kravchuk, O. Krebs, R. Kretschmer, J. Kreutzkamp, O. Kröplin, K. Krzysik, G. Kube, H. Kuehn, N. Kujala, V. Kulikov, V. Kuzminych, D. La Civita, M. Lacroix, T. Lamb, A. Lancetov, M. Larsson, D. Le Pinvidic, S. Lederer, T. Lensch, D. Lenz, A. Leuschner, F. Levenhagen, Y. Li, J. Liebing, L. Lilje, T. Limberg, D. Lipka, B. List, J. Liu, S. Liu, B. Lorbeer, J. Lorkiewicz, H.H. Lu, F. Ludwig, K. Machau, W. Maciocha, C. Madec, C. Magueur, C. Maiano, I. Maksimova, K. Malcher, T. Maltezopoulos, E. Mamoshkina, B. Manschwetus, F. Marcellini, G. Marinkovic, T. Martinez, H. Martirosyan, W. Maschmann, M. Maslov, A. Matheisen, U. Mavric, J. Meißner, K. Meissner, M. Messerschmidt, N. Meyners, G. Michalski, P. Michelato, N. Mildner, M. Moe, F. Moglia, C. Mohr, S. Mohr, W. Möller, M. Mommerz, L. Monaco, C. Montiel, M. Moretti, I. Morozov, P. Morozov, D. Mross, A MHz-repetition-rate hard X-ray free-electron laser driven by a superconducting linear accelerator, Nat. Photonics 14 (6) (2020) 391–397, http://dx.doi.org/10.1038/s41566-020-0607-z.

[2] A. Allahgholi, J. Becker, A. Delfs, R. Dinapoli, P. Goettlicher, D. Greiffenberg, B. Henrich, H. Hirsemann, M. Kuhn, R. Klanner, A. Klyuev, H. Krueger, S. Lange, T. Laurus, A. Marras, D. Mezza, A. Mozzanica, M. Niemann, J. Poehlsen, J. Schwandt, I. Sheviakov, X. Shi, S. Smoljanin, L. Steffen, J. Sztuk-Dambietz, U. Trunk, Q. Xia, M. Zeribi, J. Zhang, M. Zimmer, B. Schmitt, H. Graafsma, The adaptive gain integrating pixel detector at the European XFEL, J. Synchrotron Radiat. 26 (1) (2019) 74–82, http://dx.doi.org/10.1107/S1600577518016077.

[3] M. Porro, L. Andricek, S. Aschauer, A. Castoldi, M. Donato, J. Engelke, F. Erdinger, C. Fiorini, P. Fischer, H. Graafsma, A. Grande, C. Guazzoni, K. Hansen, S. Hauf, P. Kalavakuru, H. Klaer, M. Tangl, A. Kugel, M. Kuster, P. Lechner, D. Lomidze, S. Maffessanti, M. Manghisoni, S. Nidhi, F. Okrent, V. Re, C. Reckleben, E. Riceputi, R. Richter, A. Samartsev, S. Schlee, J. Soldat, L. Strüder, J. Szymanski, M. Turcato, G. Weidenspointner, C.B. Wunderer, The MiniSDD-based 1-Mpixel camera of the DSSC project for the European XFEL, IEEE Trans. Nucl. Sci. 68 (6) (2021) 1334–1350, http://dx.doi.org/10.1109/TNS.2021.3076602.

[4] A. Koch, M. Hart, T. Nicholls, C. Angelsen, J. Coughlan, M. French, S. Hauf, M. Kuster, J. Sztuk-Dambietz, M. Turcato, G.A. Carini, M. Chollet, S.C. Herrmann, H.T. Lemke, S. Nelson, S. Song, M. Weaver, D. Zhu, A. Meents, P. Fischer, Performance of an LPD prototype detector at MHz frame rates under synchrotron and FEL radiation, J. Instrum. 8 (11) (2013) C11001, http://dx.doi.org/10.1088/1748-0221/8/11/C11001.

[5] A.P. Mancuso, A. Aquila, L. Batchelor, R.J. Bean, J. Bielecki, G. Borchers, K. Doerner, K. Giewekemeyer, R. Graceffa, O.D. Kelsey, Y. Kim, H.J. Kirkwood, A. Legrand, R. Letrun, B. Manning, L. Lopez Morillo, M. Messerschmidt, G. Mills, S. Raabe, N. Reimers, A. Round, T. Sato, J. Schulz, C. Signe Takem, M. Sikorski, S. Stern, P. Thute, P. Vagovič, B. Weinhausen, T. Tschentscher, The single particles, clusters and biomolecules and serial femtosecond crystallography instrument of the European XFEL: initial installation, J. Synchrotron Radiat. 26 (3) (2019) 660–676, http://dx.doi.org/10.1107/S1600577519003308.

[6] A. Madsen, J. Hallmann, G. Ansaldi, T. Roth, W. Lu, C. Kim, U. Boesenberg, A. Zozulya, J. Möller, R. Shayduk, M. Scholz, A. Bartmann, A. Schmidt, I. Lobato, K. Sukharnikov, M. Reiser, K. Kazarian, I. Petrov, Materials imaging and dynamics (MID) instrument at the European X-ray free-electron laser facility, J. Synchrotron Radiat. 28 (2) (2021) 637–649, http://dx.doi.org/10.1107/S1600577521001302.

[7] U. Zastrau, K. Appel, C. Baehtz, O. Baehr, L. Batchelor, A. Berghäuser, M. Banjafar, E. Brambrink, V. Cerantola, T.E. Cowan, H. Damker, S. Dietrich, S. Di Dio Cafiso, J. Dreyer, H.-O. Engel, T. Feldmann, S. Findeisen, M. Foese, D. Fulla-Marsa, S. Göde, M. Hassan, J. Hauser, T. Herrmannsdörfer, H. Höppner, J. Kaa, P. Kaever, K. Knöfel, Z. Konôpková, A. Laso García, H.-P. Liermann, J. Mainberger, M. Makita, E.-C. Martens, E.E. McBride, D. Möller, M. Nakatsutsumi, A. Pelka, C. Plueckthun, C. Prescher, T.R. Preston, M. Röper, A. Schmidt, W. Seidel, J.-P. Schwinkendorf, M.O. Schoelmerich, U. Schramm, A. Schropp, C. Strohm, K. Sukharnikov, P. Talkovski, I. Thorpe, M. Toncian, T. Toncian, L. Wollenweber, S. Yamamoto, T. Tschentscher, The high energy density scientific instrument at the European XFEL, J. Synchrotron Radiat. 28 (5) (2021) 1393–1416, http://dx.doi.org/10.1107/S1600577521007335.

[8] R. Carley, B. Van Kuiken, L. Le Guyader, G. Mercurio, A. Scherz, SCS Instrument Review Rerport, Tech. Rep. XFEL.EU TR-2022-003, European XFEL, Holzkoppel 4, 22869 Schenefeld, Germany, 2022, http://dx.doi.org/10.22003/XFEL.EU-TR-2022-003.

[9] M. Meyer, T.M. Baumann, A. Achner, R. Boll, A.D. Fanis, P. Grychtol, M. Ilchen, T. Mazza, J. Montaño, V. Music, Y. Ovcharenko, N. Rennhack, D.E. Rivas, R. Wagner, P. Ziołkowski, D. Rolles, P. Walter, B. Erk, B. Keitel, E. Plönjes, K. Mann, S. Lange, B. Schäfer, J. Chalupský, T. Burian, K. Juranova, L. Vyšín, V. Hájková, L. Juha, The small quantum system (SQS) instrument at European XFEL: Results of commissioning and first experiments, J. Phys. Conf. Ser. 1412 (11) (2020) 112005, http://dx.doi.org/10.1088/1742-6596/1412/11/112005.

[10] A. Galler, W. Gawelda, M. Biednov, C. Bomer, A. Britz, S. Brockhauser, T.-K. Choi, M. Diez, P. Frankenberger, M. French, D. Görries, M. Hart, S. Hauf, D. Khakhulin, M. Knoll, T. Korsch, K. Kubicek, M. Kuster, P. Lang, F. Alves Lima, F. Otte, S. Schulz, P. Zalden, C. Bressler, Scientific instrument femtosecond X-ray experiments (FXE): instrumentation and baseline experimental capabilities, J. Synchrotron Radiat. 26 (5) (2019) 1432–1447, http://dx.doi.org/10.1107/S1600577519006647.

[11] N. Kujala, W. Freund, J. Liu, A. Koch, T. Falk, M. Planas, F. Dietrich, J. Laksman, T. Maltezopoulos, J. Risch, F. Dall'Antonia, J. Grünert, Hard x-ray single-shot spectrometer at the European X-ray free-electron laser, Rev. Sci. Instrum. 91 (10) (2020) 103101, http://dx.doi.org/10.1063/5.0019935.

[12] J.C.P. Koliyadu, R. Letrun, H.J. Kirkwood, J. Liu, M. Jiang, M. Emons, R. Bean, V. Bellucci, J. Bielecki, S. Birnsteinova, R. de Wijn, T. Dietze, J. E, J. Grünert, D. Kane, C. Kim, Y. Kim, M. Lederer, B. Manning, G. Mills, L.L. Morillo, N. Reimers, D. Rompotis, A. Round, M. Sikorski, C.M.S. Takem, P. Vagovič, S. Venkatesan, J. Wang, U. Wegner, A.P. Mancuso, T. Sato, Pump–probe capabilities at the SPB/SFX instrument of the European XFEL, J. Synchrotron Radiat. 29 (5) (2022) 1273–1283, http://dx.doi.org/10.1107/S1600577522006701.

[13] I. Petrov, L. Samoylova, S. Birnsteinova, V. Bellucci, M. Makita, T. Sato, R. Letrun, J. Koliyadu, R. de Wijn, A. Mazzolari, M. Romagnoni, R. Bean, A. Mancuso, A. Meents, H.N. Chapman, P. Vagovic, Absolute spectral metrology of XFEL pulses using diffraction in crystals, 2023, arXiv:2303.00072.

[14] J. Zhang, M. Andrä, R. Barten, A. Bergamaschi, M. Brückner, S. Chiriotti-Alvarez, R. Dinapoli, E. Fröjdh, D. Greiffenberg, P. Kozlowski, M. Kuster, C. Lopez-Cuenca, M. Meyer, D. Mezza, A. Mozzanica, M. Ramilli, C. Ruder, B. Schmitt, X. Shi, D. Thattil, G. Tinti, M. Turcato, S. Vetter, Design and first tests of the gotthard-II readout ASIC for the European X-ray free-electron laser, J. Instrum. 16 (04) (2021) P04015, http://dx.doi.org/10.1088/1748-0221/16/04/P04015.

[15] N. Europe, NAMC-psTimer. URL https://nateurope.com/product/namc-pstimer/.

[16] A. Hidvégi, P. Geß ler, H. Kay, K. Rehlich, C. Bohm, Timing and triggering system for the European XFEL project - a double sized AMC board, in: 2012 18th IEEE-NPSS Real Time Conference, 2012, pp. 1–3, http://dx.doi.org/10.1109/RTC.2012.6418093.

[17] S. Hauf, B. Heisen, S. Aplin, M. Beg, M. Bergemann, V. Bondar, D. Boukhelef, C. Danilevsky, W. Ehsan, S. Essenov, R. Fabbri, G. Flucke, D. Fulla Marsa, D. Göries, G. Giovanetti, D. Hickin, T. Jarosiewicz, E. Kamil, D. Khakhulin, A. Klimovskaia, T. Kluyver, Y. Kirienko, M. Kuhn, L. Maia, D. Mamchyk, V. Mariani, L. Mekinda, T. Michelat, A. Münnich, A. Padee, A. Parenti, H. Santos, A. Silenzi, M. Teichmann, K. Weger, J. Wiggins, K. Wrona, C. Xu, C. Youngman, J. Zhu, H. Fangohr, S. Brockhauser, The karabo distributed control system, J. Synchrotron Radiat. 26 (5) (2019) 1448–1461, http://dx.doi.org/10.1107/S1600577519006696.

[18] The HDF Group, Hierarchical data format, version 5, 1997-NNNN, https://www.hdfgroup.org/HDF5/.

[19] D. Khakhulin, F. Otte, M. Biednov, C. Bömer, T.-K. Choi, M. Diez, A. Galler, Y. Jiang, K. Kubicek, F.A. Lima, A. Rodriguez-Fernandez, P. Zalden, W. Gawelda, C. Bressler, Ultrafast X-ray photochemistry at European XFEL: Capabilities of the femtosecond X-ray experiments (FXE) instrument, Appl. Sci. 10 (3) (2020) http://dx.doi.org/10.3390/app10030995, URL https://www.mdpi.com/2076-3417/10/3/995.

[20] A. Mozzanica, M. Andrä, R. Barten, A. Bergamaschi, S. Chiriotti, M. Brückner, R. Dinapoli, E. Fröjdh, D. Greiffenberg, F. Leonarski, C. Lopez-Cuenca, D. Mezza, S. Redford, C. Ruder, B. Schmitt, X. Shi, D. Thattil, G. Tinti, S. Vetter, J. Zhang, The JUNGFRAU detector for applications at synchrotron light sources and XFELs, Synchrotron Radiat. News 31 (6) (2018) 16–20, http://dx.doi.org/10.1080/08940886.2018.1528429.

[21] T. Maltezopoulos, F. Dietrich, W. Freund, U.F. Jastrow, A. Koch, J. Laksman, J. Liu, M. Planas, A.A. Sorokin, K. Tiedtke, J. Grünert, Operation of X-ray gas monitors at the European XFEL, J. Synchrotron Radiat. 26 (4) (2019) 1045–1051, http://dx.doi.org/10.1107/S1600577519003795.

[22] M.R. Bionta, H.T. Lemke, J.P. Cryan, J.M. Glownia, C. Bostedt, M. Cammarata, J.-C. Castagna, Y. Ding, D.M. Fritz, A.R. Fry, J. Krzywinski, M. Messerschmidt, S. Schorb, M.L. Swiggers, R.N. Coffee, Spectral encoding of x-ray/optical relative delay, Opt. Express 19 (22) (2011) 21855–21865, http://dx.doi.org/10.1364/OE.19.021855.

[23] A. Mozzanica, A. Bergamaschi, R. Dinapoli, H. Graafsma, D. Greiffenberg, B. Henrich, I. Johnson, M. Lohmann, R. Valeria, B. Schmitt, S. Xintian, The GOTTHARD charge integrating readout detector: design and characterization, J. Instrum. 7 (01) (2012) C01019, http://dx.doi.org/10.1088/1748-0221/7/01/C01019.

[24] T. Sato, R. Letrun, H.J. Kirkwood, J. Liu, P. Vagovič, G. Mills, Y. Kim, C.M.S. Takem, M. Planas, M. Emons, T. Jezynski, G. Palmer, M. Lederer, S. Schulz, J. Mueller, H. Schlarb, A. Silenzi, G. Giovanetti, A. Parenti, M. Bergemann, T. Michelat, J. Szuba, J. Grünert, H.N. Chapman, A.P. Mancuso, Femtosecond timing synchronization at megahertz repetition rates for an x-ray free-electron laser, Optica 7 (6) (2020) 716–717, http://dx.doi.org/10.1364/OPTICA.396728.

[25] M. Diez, H. Kirchberg, A. Galler, S. Schulz, M. Biednov, C. Bömer, T. Choi, A. Rodriguez-Fernandez, W. Gawelda, D. Khakhulin, K. Kubicek, F. Lima, F. Otte, P. Zalden, R. Coffee, M. Thorwart, C. Bressler, A sensitive high repetition rate arrival time monitor for X-ray free electron lasers, Nat. Commun. 14 (2023) 2495, http://dx.doi.org/10.1038/s41467-023-38143-y.